Ultrahigh-Density Double-Atom Catalyst with Spin Moment as an Activity Descriptor for the Oxygen-Reduction Reaction

Peng Lv,[1] Wenjing Lv,[1] Donghai Wu,[1] Gang Tang,[2] Xunwang Yan,[3] Zhansheng Lu,[4,*] and Dongwei Ma[1,†,‡]

[1] *Key Laboratory for Special Functional Materials of Ministry of Education, and School of Materials Science and Engineering, Henan University, Kaifeng 475004, China*
[2] *Advanced Research Institute of Multidisciplinary Science, Beijing Institute of Technology, Beijing 100081, China*
[3] *College of Physics and Engineering, Qufu Normal University, Qufu 273165, China*
[4] *School of Physics, Henan Normal University, Xinxiang 453007, China*

(Received 28 December 2022; revised 23 April 2023; accepted 25 April 2023; published 31 May 2023)

One of the great challenges facing atomically dispersed catalysts, including single-atom catalysts (SACs) and double-atom catalysts (DACs), is their ultralow metal loading (typically less than 5 wt %), which limits their practical catalytic applications, such as in the oxygen-reduction reaction (ORR), which is crucial for hydrogen fuel cells and metal-air batteries. Although some important progress has been achieved in ultrahigh-density (UHD) SACs, reports on UHD DACs with stable uniform dispersion are still lacking. Herein, based on the experimentally synthesized M_2N_6 motif (M = Sc-Zn), we theoretically demonstrate the existence of UHD DACs, with a metal loading of >40 wt %, which are confirmed by systematic analyses of dynamic, thermal, mechanical, thermodynamic, and electrochemical stabilities. Furthermore, the ORR activities of the UHD DACs are comparable to or even better than those of their experimentally synthesized low-density counterparts, and the Fe_2N_6 and Co_2N_6 UHD DACs are located at the peak of the activity volcano with ultralow overpotentials of 0.31 and 0.33 V, respectively. Finally, the spin magnetic moment of the active center is found to be a catalytic descriptor for the ORR on DACs. Our work can stimulate the experimental exploration of ultrahigh-density DACs and provides an insight into the relationship between the ORR activity of DACs and their spin states.

DOI: 10.1103/PhysRevApplied.19.054094

I. INTRODUCTION

The four-electron oxygen-reduction reaction (ORR) is a key electrochemical reaction for renewable-energy-conversion and -storage technologies, due to its significance for metal-air batteries and proton-exchange-membrane fuel cells (PEMFCs) [1–3]. Up to now, Pt-based catalysts are the best-known ORR electrocatalysts for commercial applications [4–6]. However, the large-scale commercialization of Pt-based catalysts is significantly restricted by the low natural reserves, high cost, and limited stability of Pt. Therefore, designing and searching for alternative ORR electrocatalysts that are low cost, high activity, and have long durability are increasingly attractive, but there are great challenges ahead [7,8]. For example, a single-atom catalyst (SAC) with a uniform dispersion of transition-metal (TM) active sites coordinated with nitrogen atoms in carbon (termed as M-N-C, such as the FeN_4 SAC [9,10]) have gained much attention in the past few years [11–14].

Very recently, double-atom catalysts (DACs) have emerged as a frontier in heterogenous electrocatalysis due to their synergetic dual atomic sites, which can endow DACs with many intrinsic advantages compared with SACs for multiple-step coupled electron–proton-transfer reactions in electrocatalysis [15–17]. To be specific, for the ORR, the dual atomic sites can facilitate dissociation of the O—O bond of intermediates tending to adopt the side-on adsorption configuration, which favors the desirable four-electron ORR and hinders the two-electron ORR, thereby promoting the energy efficiency of the ORR process in PEMFCs or metal-air batteries and enhancing the stability of catalysts [18–30]. Among the various DACs for the ORR, those with each TM coordinated to four N atoms in a carbon sheet [termed as M_2N_6 DAC, as shown in Fig. S1(a) within the Supplemental Material [31]] have gained particular attention [18,23–29,32,33], for which the basic structural motif, M_2N_6, is shown in Fig. 1(a). Combining experimental and theoretical simulations, the $FeMnN_6$, $FeCoN_6$, $FeNiN_6$, and $FeZnN_6$ DACs for the

---

[*] zslu@htu.edu.cn
[†] madw@henu.edu.cn
[‡] dwmachina@126.com

ORR are thoroughly investigated, and these systems outperform their corresponding SAC counterparts and even the Pt/C catalyst [23–26,28,29]. For example, electronic synergies between Fe and Mn in $\mathrm{FeMnN_6}$ deliver better durability and excellent ORR performance (half-wave potentials are 0.928 and 0.804 V under alkaline conditions and in acidic media, respectively) than those of $\mathrm{FeN_4}$ and $\mathrm{MnN_4}$ SACs and commercial Pt/C catalyst [24]. In addition, besides the ORR, $M_2\mathrm{N}_6$ DACs are also theoretically and experimentally demonstrated to be efficient for electrocatalytic $\mathrm{CO_2}$ reduction and other reactions [34–39].

On the other hand, one of the most significant challenges facing atomically dispersed catalysts is their ultralow active-site density (typically less than 5 wt %) [23–25,27,34,39–43], which leads to their overall poor catalytic performance and limits future industrialization. For example, for the $\mathrm{MnFeN_6}$ DAC mentioned above, the contents of Fe and Mn are only 2.3 and 1.6 wt %, respectively [24]. Excitingly, very recently, there have already been some breakthroughs in synthesizing ultrahigh-density (UHD) SACs [44–48]. A multilayer stabilization strategy is used to construct SACs with metal loadings up to 16 wt % [49]. A versatile approach combining impregnation and two-step annealing can successfully synthesize 15 metals on chemically distinct supports with metal contents up to 23 wt % [50]. The meal loading of SACs can even reach up to about 40 wt % by means of a graphene quantum-dot-assisted synthesis strategy [51]. However, with the advantages of DACs compared with SACs in mind, no UHD DACs have been reported to date; these are the focus of the present study.

Herein, starting from the $M_2\mathrm{N}_6$ motif shown in Fig. 1(a), we try to construct UHD DACs [Fig. 1(a)] with as few C atoms as possible as glue, to reach a metal loading of >40 wt %, corresponding to 14 at %. For the active center, all the 3*d* TMs (Sc-Zn) with small atomic radii are considered, as inspired by experimental reports [24,26,34,35]. Among various UHD DAC candidates, ten are screened that exhibit excellent dynamic, thermal, mechanical, thermodynamic, and electrochemical stabilities, comparable to those of the corresponding low-density (LD) systems [see the atomic models in Fig. S1(b) within the Supplemental Material [31]]. Furthermore, the ORR reaction mechanism is investigated for the UHD DACs and their corresponding LD DACs [Fig. S1(b) within the Supplemental Material [31]]. Finally, the relationship between the ORR catalytic activity of the considered DACs and their spin magnetic moment is investigated and uncovered.

II. COMPUTATIONAL DETAILS

All spin-polarized computations are carried out by using the generalized gradient approximation (GGA) method with the Perdew-Burke-Ernzerhof (PBE) functional [52] based on density-functional theory (DFT) implemented in the Vienna *ab initio* simulation package (VASP) [53,54], in which the van der Waals correction proposed by Grimme *et al.* (DFT + D3) is chosen [55]. The plane-wave basis set with a cutoff energy of 500 eV is employed. A vacuum layer of about 16 Å is used to avoid interactions between periodic images for all calculations. The convergence thresholds of the total energy and the Hellmann-Feynman force are 10^{-7} eV and 0.0005 eV/Å, respectively. For structural optimization of the primitive cell, various magnetic states are considered and relaxed by the 8 × 8 × 1 Monkhorst-Pack meshes, and the optimized lattice parameters of the lowest-energy structures are presented in Table S1 within the Supplemental Material [31], with the corresponding atomic configurations in Fig. S1(c) within the Supplemental Material [31]. The phonon dispersions are calculated with the finite-displacement method by using the PHONOPY code [56]. The *ab initio* molecular dynamics (AIMD) simulations for the UHD DAC supercells (2 × 2 × 1) are performed based on the *NVT* ensemble with a time step of 2 fs and total time of 10 ps. The simulated scanning tunneling microscopy (STM) images are obtained using Tersoff-Hamann theory [57].

The binding energy (E_b), dissolution potential (U_{diss}, versus a standard hydrogen electrode), and formation energy (E_{form}) of UHD DACs and corresponding LD DACs can be defined as

$$E_b = E(\mathrm{total}) - E(\mathrm{CN}) - \mu(M_1) - \mu(M_2), \tag{1}$$

$$U_{\mathrm{diss}} = {U_{\mathrm{diss}}}^{\circ}(\mathrm{metal, bulk}) - E_b/(eN_eN_M), \tag{2}$$

$$E_{\mathrm{form}} = E(\mathrm{total}) - 6\mu(\mathrm{N}) - 6\mu(\mathrm{C}) - \mu(M_1) - \mu(M_2), \tag{3}$$

where E(total) and E(CN) are the total energies of the DAC system and CN composite, respectively; $\mu(M_1)$, $\mu(M_2)$, μ(N), and μ(C) are the chemical potentials of the species involved, which are taken from the bulk metals, $\mathrm{N_2}$ molecules, and graphene; ${U_{\mathrm{diss}}}^{\circ}$(metal, bulk) and N_e are the standard dissolution potential (pH = 0) of bulk metal in aqueous solution and the number of electrons involved in dissolution, respectively, which are taken from previous work [58,59] and are listed in Table S4 within the Supplemental Material [31]. N_M indicates the number of metal atoms. N_M is two for the current DAC system [60].

The in-plane Young's modulus (E_x, E_y), Poisson ratio (ν_{xy}, ν_{yx}), and shear modulus (G) along the armchair (x) and zigzag (y) directions for UHD DACs can be calculated by [61]

$$E_x = (C_{11}C_{22} - C_{12}C_{21})/C_{22}, \tag{4}$$

$$E_y = (C_{11}C_{22} - C_{12}C_{21})/C_{11}, \tag{5}$$

$$\nu_{xy} = C_{21}/C_{22}, \tag{6}$$

$$\nu_{yx} = C_{12}/C_{11}, \tag{7}$$

$$G = C_{66}. \tag{8}$$

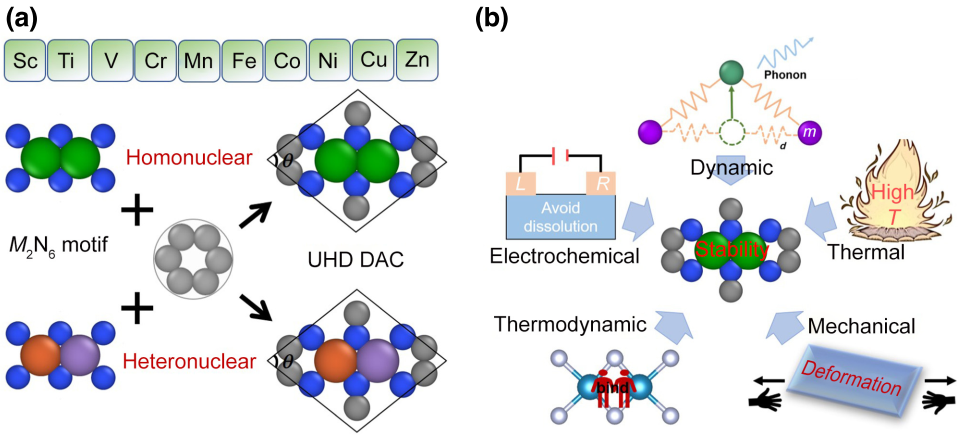

FIG. 1. (a) Schematic depiction of the M_2N_6 UHD DAC construction ($M = $ Sc, Ti, V, Cr, Mn, Fe, Co, Ni, Cu, and Zn) from the experimental M_2N_6 motif with the bonding of carbon atoms, including homonuclear and heteronuclear DACs. (b) Five considered stabilities for M_2N_6 UHD DACs: dynamic, thermal, mechanical, thermodynamic, and electrochemical stabilities.

For the ORR-related calculations, standard conventional cells of various UHD DACs are used as the electrocatalysts, and the $5 \times 4 \times 1$ and $12 \times 10 \times 1$ Monkhorst-Pack meshes are adopted for structural optimization and calculation of densities of states (DOS), respectively. The convergence thresholds of the total energy and the Hellmann-Feynman force are 10^{-5} eV and 0.03 eV/Å, respectively.

The free-energy change (ΔG) in acidic medium (pH = 0) for each elementary reaction step is calculated based on the computational hydrogen electrode model [62–64], according to

$$\Delta G = \Delta E + \Delta E_{\mathrm{ZPE}} - T\Delta S, \tag{9}$$

where ΔE is the reaction energy from DFT calculations. ΔE_{ZPE} and $T\Delta S$ ($T = 298.15$ K) are the contributions of the zero-point energy and entropy to ΔG, respectively. E_{ZPE} and TS for the free molecules are taken from the NIST database [65], and those of the adsorbed species are obtained based on the vibrational frequencies calculated with the VASPKIT code [66]. The reaction step with $\Delta G_{\max}$ is the potential-determining step.

The ORR is investigated in acidic medium (pH = 0), and the corresponding elementary reaction steps along pathway A, pathway B, and pathway C for the ORR can be described as

$$^{*}{+}O_2 + H^+ + e^- \rightarrow {}^{*}OOH, \tag{10A}$$

$$^{*}{+}O_2 + H^+ + e^- \rightarrow {}^{*}O^{*}OH, \tag*{(10A,10C)}$$

$$^{*}OOH + H^+ + e^- \rightarrow {}^{*}O + H_2O, \tag{11A}$$

$$^{*}O^{*}OH + H^+ + e^- - \rightarrow {}^{*}O + H_2O, \tag{11B}$$

$$^{*}O^{*}OH + H^+ + e^- \rightarrow {}^{*}OH^{*}OH, \tag{11C}$$

$$^{*}O + H^+ + e^- \rightarrow {}^{*}OH, \tag*{(12A,12B)}$$

$$^{*}OH^{*}OH + H^+ + e^- \rightarrow {}^{*}OH + H_2O, \tag{12C}$$

$$^{*}OH + H^+ + e^- \rightarrow {}^{*}{+}H_2O. \tag*{(13A,13B,13C)}$$

The Gibbs adsorption free energy of the intermediates [*OH, *OOH (*O*OH), *OH*OH, and *O] can be evaluated by

$$\Delta G({}^{*}OH) = G({}^{*}OH) + 1/2G(H_2) - G^{*} - G(H_2O), \tag{14}$$

$$\Delta G({}^{*}OOH) = G({}^{*}OOH) + 3/2G(H_2) - G^{*} - 2G(H_2O), \tag{15}$$

$$\Delta G({}^{*}O^{*}OH) = G({}^{*}O^{*}OH) + 3/2G(H_2) - G^{*} - 2G(H_2O), \tag{16}$$

$$\Delta G({}^{*}OH^{*}OH) = G({}^{*}OH^{*}OH) + G(H_2) - G^{*} - 2G(H_2O), \tag{17}$$

$$\Delta G({}^{*}O) = G({}^{*}O) + G(H_2) - G^{*} - {}^{*}G(H_2O). \tag{18}$$

According to the above ΔG values, and setting $\Delta G(O_2) = 4.92$ eV and $\Delta G(H_2O) = 0$ eV, we can obtain the free-energy changes (ΔG_x, for step $x = 1$–4) and equilibrium potential (U_x, $x = 1$–4) as follows:

$$\Delta G_1 = -eU_1 = \Delta G({}^{*}OOH) - 4.92, \tag{19A}$$

$$\Delta G_1 = -eU_1 = \Delta G({}^{*}O^{*}OH) - 4.92, \tag*{(19B,19C)}$$

$$\Delta G_2 = -eU_2 = \Delta G({}^{*}O) - \Delta G({}^{*}OOH), \tag{20A}$$

$$\Delta G_2 = -eU_2 = \Delta G({}^{*}O) - \Delta G({}^{*}O^{*}OH), \tag{20B}$$

$$\Delta G_2 = -eU_2 = \Delta G(^*\mathrm{OH}^*\mathrm{OH}) - \Delta G(^*\mathrm{O}^*\mathrm{OH}), \quad (20\mathrm{C})$$

$$\Delta G_3 = -eU_3 = \Delta G(^*\mathrm{OH}) - \Delta G(^*\mathrm{O}), \quad (21\mathrm{A},21\mathrm{B})$$

$$\Delta G_3 = -eU_3 = \Delta G(^*\mathrm{OH}) - \Delta G(^*\mathrm{OH}^*\mathrm{OH}), \quad (21\mathrm{C})$$

$$\Delta G_4 = -eU_4 = -\Delta G(^*\mathrm{OH}), \quad (22\mathrm{A},22\mathrm{B},22\mathrm{C})$$

where A, B, and C indicate pathway A, pathway B, and pathway C for the ORR, respectively. Then the overpotential (η_{ORR}, V) is defined by

$$\eta_{\mathrm{ORR}} = (\Delta G_{\max}/e) + 1.23. \quad (23)$$

Standard GGA simulations usually underestimate the solvation effect, which affects the free energies of the ORR under practical conditions. The continuum solvation model [67] is used to investigate the solvation effect for the ORR. The solvation energies for different adsorbed species are shown in Table S6 within the Supplemental Material [31]. These values from the continuum solvation model are all negative, indicating that the solvent can stabilize the adsorbates in solution. Also, it is noted that our calculation values are comparable to those of previous works [18,59,68]. We also study the solvation effect of explicit water on the ORR by combining the force-field molecular dynamics simulation implemented in LAMMPS [69,70], *ab initio* molecular dynamics simulation in VASPsol [67], and static structural optimization. It is found that the solvation energies obtained with the continuum solvation model in VASPsol are comparable to those from our explicit model and those of previous works [18,68,71]. Moreover, the explicit solvation effect does not alter the optimal reaction pathways for the ORR on both UHD and LD DACs (see Note S1 with corresponding figures and tables in the Supplemental Material [31]).

III. RESULTS AND DISCUSSION

A. Morphologies of UHD DACs

Stimulated by the experimental LD DAC [Fig. S1(a) within the Supplemental Material [31]], we design an alternative two-dimensional (2D) material [i.e., the UHD DAC given in Fig. 1(a)] by significantly reducing the surrounding carbon atoms of the dual-metal active center. As seen in Fig. 1(a), the lattice structure of the $M_2\mathrm{N}_6$ UHD DACs is constructed by fixing the $M_2\mathrm{N}_6$ motif to six C atoms located at the corners of a primitive cell, which realize a minimum cell containing a pair of TM atoms (TM = Sc-Zn). Thus, the geometric structure of the active center for the designed UHD DACs is the same as that of experimentally prepared LD DACs, but the former achieves an unprecedently ultrahigh density of active centers with metal loadings up to 36–46 wt % for DACs, which are close to the recently reported ultrahigh-density Ir-N-C SAC (~40 wt %) [51]. From the viewpoint of atomic metal percentage [72], here, the UHD DACs present high metal contents of 14.3 at %, about 4 times larger than that of the Ir-N-C SAC (3.8 at %) [51]. For structural optimization, the optimized lattice parameters of the lowest-energy structures are presented in Table S1 within the Supplemental Material [31], with the corresponding atomic configurations in Fig. S1(c) within the Supplemental Material [31]. For all cases, the systems have the 2D rhombus lattice of the primitive cell, while they have a 2D rectangular conventional cell, dissimilar to the well-known lattice symmetry of graphene. The homonuclear (heteronuclear) UHD DAC structures are in the *Cmmm* (*Amm*2) space group with D_{2h} (C_{2v}) point-group symmetry, which both belong to the orthorhombic phase. In contrast, the theoretical model of experimentally synthesized LD DACs is also built by embedding the same $M_2\mathrm{N}_6$ active center in 3×6 rectangular supercells [Fig. S1(b) within the Supplemental Material [31]] for simulations.

B. Dynamic, thermal, mechanical, thermodynamic, and electrochemical stabilities of UHD DACs

We comprehensively examine their stabilities with respect to five aspects: dynamic, thermal, mechanical, thermodynamic, and electrochemical stabilities [Fig. 1(b)]. The constructed UHD DAC is considered stable if it meets all the stability criteria (Fig. S2 within the Supplemental Material [31]). First, the dynamic stability of the homonuclear $M_2\mathrm{N}_6$ UHD DACs is verified by calculating their phonon dispersions, which describe the dispersion relationships of lattice vibrations and are usually identified as the decisive factor in a material's stability. From Fig. 2(a) and Fig. S3 within the Supplemental Material [31], we find that only homonuclear $\mathrm{Mn_2N_6}$, $\mathrm{Fe_2N_6}$, $\mathrm{Co_2N_6}$, and $\mathrm{Ni_2N_6}$ UHD DACs are dynamically stable, as indicated by the absence of obvious imaginary phonon frequencies. Small atomic radii of Mn, Fe, Co, and Ni correspond to relatively small lattice constants and compact lattice interactions [73] of UHD DACs, which are responsible for the dynamic stability of homonuclear $\mathrm{Mn_2N_6}$, $\mathrm{Fe_2N_6}$, $\mathrm{Co_2N_6}$, and $\mathrm{Ni_2N_6}$ UHD DACs. Based on this result, it is expected that the heteronuclear UHD DACs formed by the pairwise combination of these four elements will also have good dynamic stability. Thus, we also investigate the phonon dispersions of six heteronuclear $M_2\mathrm{N}_6$ UHD DACs, i.e., $\mathrm{MnFeN_6}$, $\mathrm{MnCoN_6}$, $\mathrm{MnNiN_6}$, $\mathrm{FeCoN_6}$, $\mathrm{FeNiN_6}$, and $\mathrm{CoNiN_6}$ (Fig. S3 within the Supplemental Material [31]). Like their corresponding homonuclear ones, they also possess great dynamic stability without any imaginary frequencies. It is noted that all the UHD DAC structures have 52 phonon vibrational modes, of which there are 3 acoustic modes and 49 optical modes. Through group-theory analysis, the irreducible representation of the optical branches at the Brillouin zone with Raman (R) and infrared (IR) labels for the homonuclear and heteronuclear UHD DAC structures are

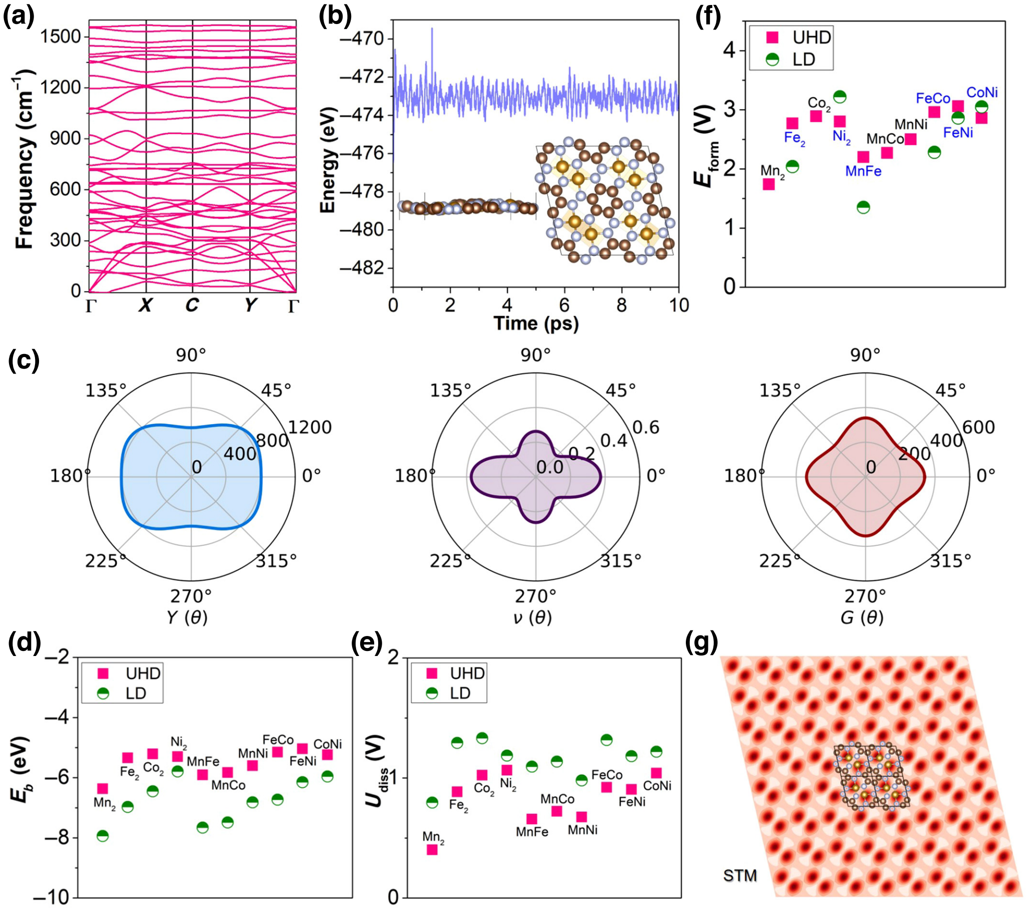

FIG. 2. (a) Phonon dispersions and (b) total-free-energy fluctuation during AIMD simulations for the Fe_2N_6 UHD DAC. In (b), AIMD simulation is performed at 500 K for 10 ps with a time step of 2 fs. Side and top views of the atomic configuration at 10 ps are shown as insets. (c) 2D projection in polar coordinates of the Young's modulus (Y, GPa), Poisson ratio (ν), and shear modulus (G) of Fe_2N_6 UHD DAC. (d) Binding energies (E_b) and (e) dissolution potentials (U_{diss}) of double-metal atoms for ten considered M_2N_6 UHD DACs with dynamic stability and their corresponding LD DACs. (f) Formation energies (E_{form}) for ten considered M_2N_6 UHD DACs with dynamic stability and some corresponding experimental LD DACs. (g) Simulated STM image for the Fe_2N_6 UHD DAC with a bias voltage of 1.0 V for 8 × 8 supercells. Tip is considered to be separated from the sample by a vacuum barrier width of 3.5 Å.

as follows: $\Gamma_{\text{optic}}(\text{homonuclear}) = 7A_g$ (R) $+ 2A_u + 7B_{1g}$ (R) $+ 4B_{1u}$ (IR) $+ 3B_{2g}$ (R) $+ 6B_{2u}$ (IR) $+ 4B_{3g}$ (R) $+ 6B_{3u}$ (IR); $\Gamma_{\text{optic}}(\text{heteronuclear}) = 13A_1$ (R, IR) $+ 6A_2$ (R) $+ 7B_1$ (R, IR) $+ 13B_2$ (R, IR). We hope that future Raman and IR Brillouin spectroscopy measurements will test and verify the accuracy of the calculations in our theoretical modeling.

Furthermore, AIMD simulations are performed to check the thermal stability, under ambient conditions, of these ten M_2N_6 UHD DACs with dynamic stability. Note that their total free energy shows only periodic oscillations near the equilibrium state during the entire simulation period of 10 ps at 500 K [Fig. 2(b) and Fig. S4 within the Supplemental Material [31]]. Simulation snapshots of the M_2N_6 UHD DACs also show their structural integrity at 10 ps, implying their thermal stability. In addition, we calculate the elastic constants (Table S3 within the Supplemental Material [31]) of M_2N_6 UHD DACs using the finite-difference method [74] by assuming a thickness of 3.34 Å on the basis of graphene's thickness [75] to check their mechanical stability. Significantly, these values satisfy the requirements of the mechanical stability criterion [76,77] of a 2D material, i.e., $C_{11} \times C_{22} - {C_{12}}^2 > 0$ and $C_{66} > 0$. The in-plane Young's modulus (Y, GPa), Poisson ratio (ν), and shear modulus (G, GPa) are obtained from the elastic constants and are summarized in Table S3 within the Supplemental Material [31]. Also, the 2D directional projection in polar coordinates of the Young's modulus, Poisson ratio, and shear modulus of Fe_2N_6 UHD DAC are displayed in Fig. 2(c), and those for other systems are illustrated in Fig. S5 within the Supplemental Material [31]. The mechanical results in Fig. 2(c) and Fig.

S5 and Table S3 within the Supplemental Material [31] show that the in-plane Young's modulus and Poisson ratio along the armchair direction are larger than those along the zigzag direction, revealing the moderate anisotropy of the mechanical properties. Also, it is noted that the Young's modulus of all the UHD DACs are much smaller than that of graphene (~1000 GPa) [75,78], indicating that these UHD DACs are softer than well-known graphene and suitable for strain-tunable catalysis [79].

The thermodynamic stability of ten UHD DACs is examined by the binding energy (E_b), as shown in Fig. 2(d) and Table S4 within the Supplemental Material [31]. The more-negative E_b values indicate that stronger chemical bonds form between the metal atoms and the coordinated N atoms. We can see that the E_b values for all ten UHD DACs are more negative than -5 eV, which can effectively prevent the diffusion and aggregation of metal atoms, promising high thermodynamic stability of the whole system. For comparison, the E_b values for the corresponding LD DACs are also calculated, and the E_b values of UHD DACs are only slightly more positive than those of the corresponding LD DACs, suggesting that the high-density metal loading will not affect the thermodynamic stability of current DAC systems.

The electrochemical stability of an electrocatalyst is one of the key factors for its practical application in an electrochemical environment [59]. According to its definition in Sec. II, the more-positive dissolution potential (U_diss) suggests that the metal dimer strongly binds with coordinated atoms in the UHD DAC system, and the dissolution of metal atoms can be avoided under acidic conditions ($\mathrm{pH} = 0$). To this end, we calculate U_diss of the above ten UHD DAC systems, as illustrated in Fig. 2(e) and Table S4 within the Supplemental Material [31]. Here, we use the range of $U_\mathrm{diss} > 0$ V to measure the electrochemical stability, which is a valid evaluation criterion that is widely used in the literature [59,80]. Given that all ten DAC systems have positive U_diss values, the metal dimers in the corresponding UHD DACs (Mn_2N_6, Fe_2N_6, Co_2N_6, Ni_2N_6, $MnFeN_6$, $MnCoN_6$, $MnNiN_6$, $FeCoN_6$, $FeNiN_6$, and $CoNiN_6$) with dynamic, thermal, mechanical, and thermodynamic stability can survive under the experimental electrochemical conditions, suggesting their excellent electrochemical stability.

C. Synthesis feasibility and electronic properties of UHD DACs

Then, the feasibility of the experimental realization of these ten UHD DACs is explored by calculating the formation energies (E_form), as described in Sec. II. As shown in Fig. 2(f) and Table S4 within the Supplemental Material [31], their E_form values range from about 1.7 to 3.1 eV and are generally smaller than those of other kinds of M_2N_6 catalysts with double MN_3 groups [81,82]. We also observe that the formation energies of Ni_2N_6, $FeNiN_6$, and $CoNiN_6$ UHD DACs are lower than or comparable to those of the corresponding synthesized ones with low metal contents [23,28,29,39,43]. Notably, the values of E_form depend on the chemical potentials of the species involved, which, in turn, depend on the experimental conditions. Therefore, it is the relative values of E_form that determine the formation probability of a specific system among various ones, and it is also expected that all the proposed UHD DAC systems with dynamic, thermal, mechanical, thermodynamic, and electrochemical stabilities can be suitably synthesized in experiments. Moreover, the calculated E_form values of UHD DACs also indicate the thermodynamic stability of the N-N motif and suppression of N_2 gas formation in the UHD DACs because all these values are lower than that of the experimentally synthesized Ni_2N_6 LD DAC (3.22 eV) [39]. Hence, we also theoretically predict the STM images of these ten stable UHD DACs with 8×8 supercells for future experimental identification, as shown in Fig. 2(g) and Fig. S6 within the Supplemental Material [31]. It is easy to recognize and correlate them with the corresponding atomic structure of metal dimers, while the C and N atoms are difficult to identify because they are lighter, and thus, brighter than the metal ones.

We further investigate the electronic properties of these ten stable UHD DACs, including the electron-localization function (ELF) and DOS. The bonding characters can be effectively characterized by the ELF. As shown in Fig. S7 within the Supplemental Material [31], the electrons are more localized around C and N atoms with larger ELF values, but more delocalized around metal atoms with smaller ELF values, indicating strong covalent-bonding characteristics for C-C, C-N, N-N, and Fe-N interactions and metallic bonding features of metal dimers, which are responsible for the good stability of the UHD DACs. Importantly, the calculated total DOS (TDOS) and partial DOS (PDOS) based on the PBE and HSE06 functionals [83] presented in Figs. S8 and S9 within the Supplemental Material [31] suggest the metallic conductivity feature of all stable UHD DACs, which is beneficial for charge transfer during the electrocatalytic ORR process. Finally, for most of the systems, there are large spin magnetic moments localized on the anchored metal atoms, which benefit the effective adsorption and activation of oxygenated intermediates [84–86]. However, the spin magnetic moments of the embedded Ni atoms are fully quenched in the Ni_2N_6 and $CoNiN_6$ UHD DACs, probably due to charge transfer and electronic state coupling.

D. Scaling relationship for adsorption of key intermediates

Following the comprehensive assessment of the overall stabilities and electronic properties of ten UHD DACs, we investigate their ORR catalytic activity, as well as that of the corresponding LD DACs. Considering the dual-metal sites of DACs, three reaction pathways for the ORR are considered under acidic conditions (pH = 0). The traditional ORR pathway over the catalysts is shown in Fig. 3(a): the protonation of *OOH to produce the first H_2O molecule and the continuous hydrogenation of the remaining *O atom to yield the second H_2O molecule (pathway A). Moreover, the dual-metal sites may facilitate breaking of the O—O bond of *OOH, as described in Fig. 3(a) to drive the ORR to follow pathway B or pathway C [19,87]. All three pathways are considered for the ORR to obtain the most energetically feasible one.

In fact, there are two mechanisms for the first electron-transfer process of the ORR [88]. One is that the process of short-range electron transfer to adsorbed O_2 occurs in the inner Helmholtz plane (the ET IHP mechanism), for which O_2 is protonated on the catalyst surface to form *OOH. Another is that the process of long-range electron transfer to nonadsorbed O_2 occurs in the outer Helmholtz plane (the ET OHP mechanism), for which O_2 is protonated in the electrolyte and subsequently adsorbs at the active site as *OOH. However, the ET IHP mechanism usually occurs on Pt-based noble-metal catalysts. For the SACs and DACs, the ET OHP mechanism is usually considered to be the relevant one [11,26]. Thus, we focus on the latter ET OHP mechanism, which does not rely on the direct adsorption of O_2 onto the catalyst surface and the initial stage for the ORR is gas-phase O_2.

First, we investigate the adsorption of key intermediates, including *O, *OOH, *O*OH, *OH*OH, and *OH, and the scaling relationship between their binding strengths [*O and *OOH versus *OH (pathway A); *O and *O*OH versus *OH (pathway B); *OH*OH and *O*OH versus *OH (pathway C)]. From Figs. 3(b)–3(d), we can see that for UHD DACs pathway A exhibits an excellent linear scaling relationship between the binding strengths of the oxygenated intermediates, with $R^2 = 0.99$ and 0.98 for $\Delta G(^*\mathrm{O})$ and $\Delta G(^*\mathrm{OOH})$ versus $\Delta G(^*\mathrm{OH})$, respectively. For pathway B, the binding strengths of *O and *OH are also well correlated with $R^2 = 0.98$. However, the binding strengths between *O*OH or *OH*OH and *OH for pathways B and C display relatively poor linear relationships (with $R^2 < 0.71$), which can help to achieve better ORR activity due to the deviation from the linear scaling relationship. Moreover, this poor scaling relationship can be ascribed to the different adsorption modes of *O*OH and *OH*OH,

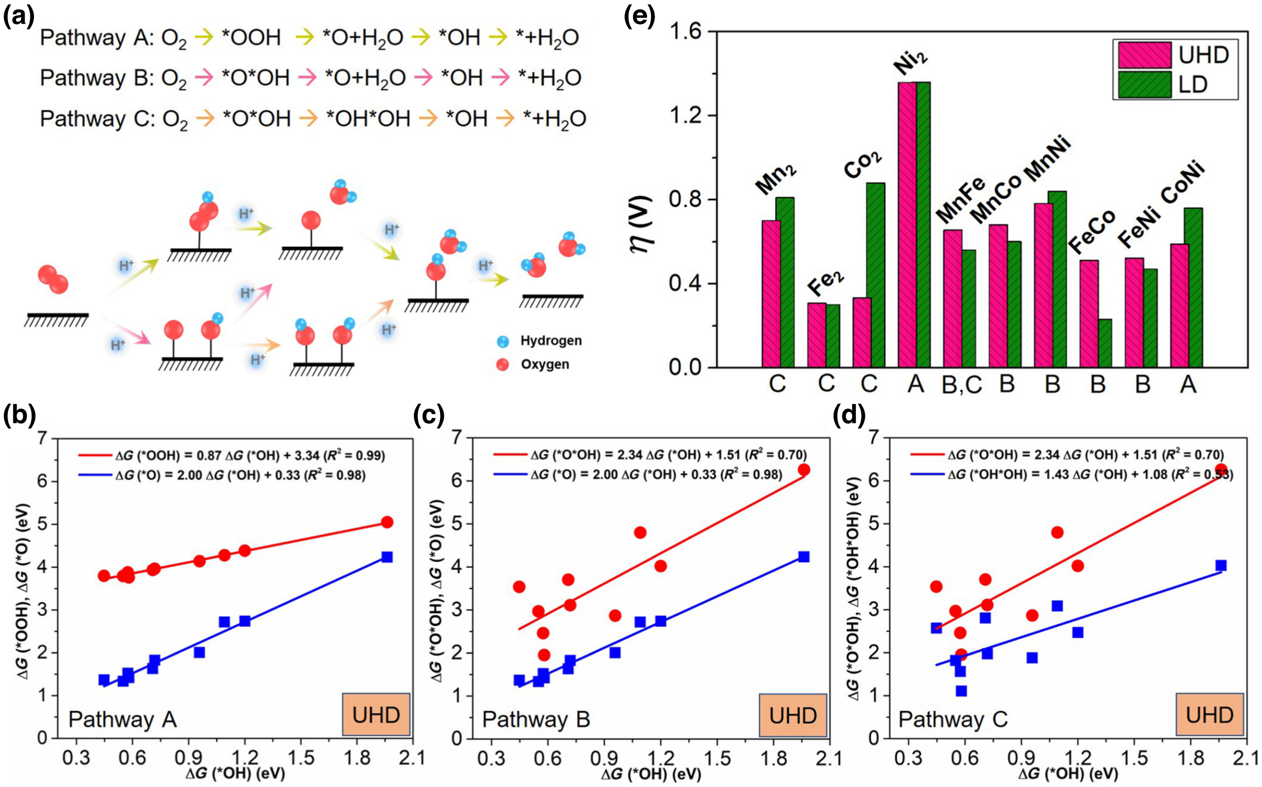

FIG. 3. (a) Schematic depiction of three possible reaction pathways for the ORR at pH = 0. Scaling relationship between the Gibbs adsorption free energy of the oxygenated intermediates for (b) pathway A, (c) pathway B, and (d) pathway C over the corresponding UHD DACs. (e) Overpotentials (η_{ORR}) of the ORR through the optimal reaction pathway (A, B, or C) over corresponding UHD and LD DACs.

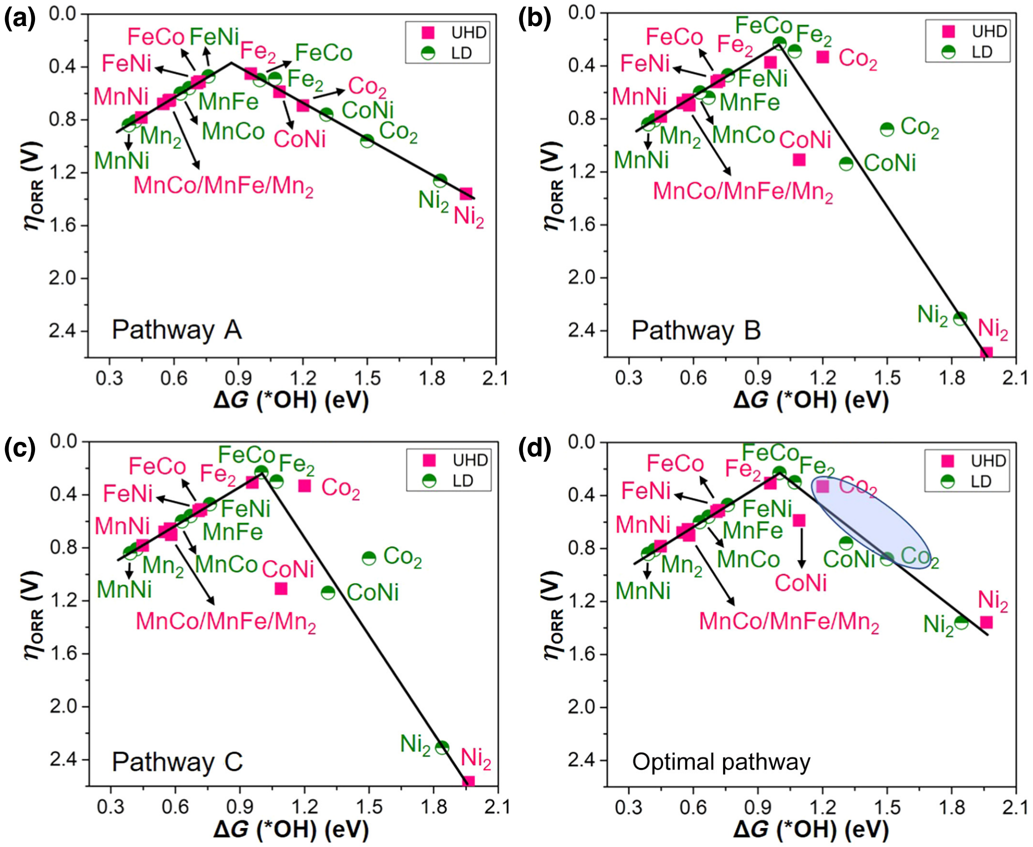

FIG. 4. Volcano plots for η_{ORR} as a function of the Gibbs adsorption free energy, ΔG(*OH), for (a) pathway A, (b) pathway B, (c) pathway C, and (d) optimal pathway. Pink and green marks represent the UHD and LD DACs, respectively.

both of which bind to the active sites through two metal atoms, compared with *OH binding through one metal atom (Fig. S10 within the Supplemental Material [31]). The flexible dual-atom active sites inducing decoupled binding strength between key intermediates are observed in other reactions, such as electrocatalytic CO_2 reduction and N_2 reduction [89–91]. Notably, for the LD DAC systems, comparatively, the scaling relationship between the binding strengths of key intermediates (Fig. S11 within the Supplemental Material [31]) have similar linear trends to the above UHD DACs.

E. ORR catalytic activity of UHD DACs

For the three ORR pathways, the reaction free-energy diagrams on UHD DACs under different potentials are shown in Figs. S12–S14 within the Supplemental Material [31], and the theoretical overpotentials (η_{ORR}) for the most favorable pathway are summarized in Fig. 3(e). We can observe that the homonuclear Mn_2N_6, Fe_2N_6, and Co_2N_6 UHD DACs prefer pathway C, in which the O—O bond of *OOH is broken and the *OH*OH species is formed, with each O atom binding to one metal atom. The heteronuclear UHD DACs (except $CoNiN_6$ with pathway A) tend to adopt pathway B, where dissociated *OOH, i.e., *O*OH, is reduced to *O. Among them, Fe_2N_6 and Co_2N_6 UHD DACs have the smallest η_{ORR} values of 0.31 and 0.33 V, respectively, along optimal pathway C, delivering the highest ORR activity among all the UHD DACs. Notably, the η_{ORR} values of Fe_2N_6 and Co_2N_6 UHD DACs are smaller than that for the state-of-the-art commercial Pt/C catalyst (0.45 V) [1,92]. Moreover, interestingly, the Fe- and Co-based heteronuclear UHD DACs also have relatively good catalytic activity, for which the $MnFeN_6$, $MnCoN_6$, $FeCoN_6$, $FeNiN_6$, and $CoNiN_6$ UHD DACs possess η_{ORR} values of 0.66, 0.68, 0.51, 0.52, and 0.59 V, respectively. For comparison, we also investigate the ORR activity over the corresponding LD DACs, for which the free-energy diagrams are presented in Figs. S15–S17 within the Supplemental Material [31], and the η_{ORR} values of the optimal pathways are also summarized in Fig. 3(e). We can see the η_{ORR} values for all the UHD DACs (except Co_2N_6) are comparable with those of the corresponding LD DACs, indicating that the UHD DACs can maintain the intrinsic ORR activity of the active centers. Interestingly, the Co_2N_6 UHD DAC even exhibits much higher ORR activity than that of its LD DAC counterpart. More significantly, $FeMnN_6$, $FeCoN_6$, $FeNiN_6$, and

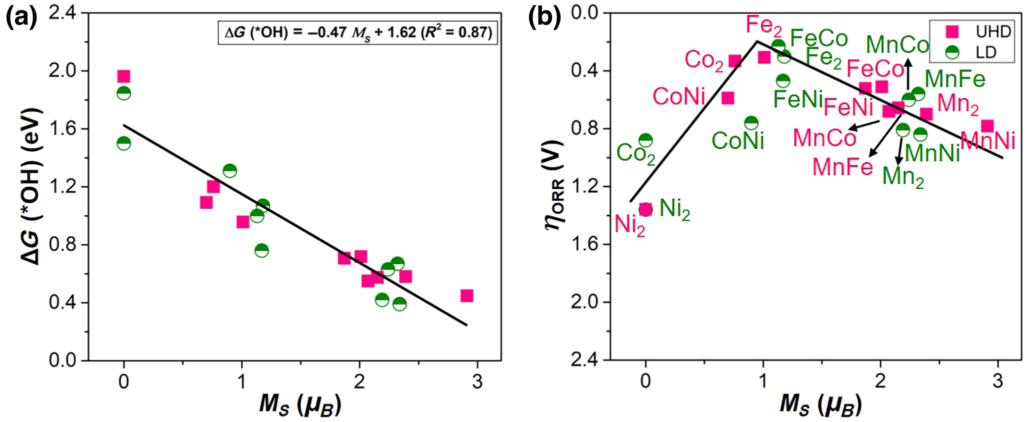

FIG. 5. (a) Scaling relationship between the Gibbs adsorption free energy of *OH [$\Delta G(^*\mathrm{OH})$] for the optimal pathway and local spin magnetic moments (M_S) for the metal atom that anchors *OH. (b) Volcano plots for η_{ORR} for the optimal pathway as a function of local spin magnetic moments for the metal atoms that anchor *OH. Pink and green marks represent UHD and LD DACs, respectively.

$\mathrm{FeZnN_6}$ DACs are determined to exhibit excellent catalytic performances for the ORR [23–26,28,29]. Overall, the excellent stabilities and ORR catalytic activities render the proposed UHD DACs promising ORR electrocatalysts with ultrahigh-density active sites available.

Moreover, we consider competing reactions on the UHD DACs, including the two-electron ORR and the hydrogen-evolution reaction. The results show that most of the UHD DACs have good selectivity for the four-electron ORR toward H_2O (for details, see Table S5 within the Supplemental Material [31]).

To better understand the ORR catalytic trend, η_{ORR} as a function of $\Delta G(^*\mathrm{OH})$ is plotted in Fig. 4. It can be found that, for pathway A [Fig. 4(a)], pathway B [Fig. 4(b)], and pathway C [Fig. 4(c)], when $\Delta G(^*\mathrm{OH})$ reaches about 0.9, 1.0, and 1.0 eV, respectively, the DAC systems possess the highest ORR catalytic activities (lowest η_{ORR}), and weaker or stronger binding of *OH on the active sites will lead to the deteriorated ORR activities. Consequently, a volcanic relationship between η_{ORR} and $\Delta G(^*\mathrm{OH})$ can be observed for all the reaction pathways. Thus, $\Delta G(^*\mathrm{OH})$ can serve as an effective ORR activity descriptor for the studied DAC systems. Moreover, for the optimal reaction pathways of each DAC [Fig. 4(d)], the appropriate binding strength of *OH on $\mathrm{Fe_2N_6}$ and $\mathrm{Co_2N_6}$ UHD DACs prompts the equilibrium between oxygenated-species activation and catalyst recovery and then results in the highest activity among all the UHD DACs.

F. Spin as a universal descriptor for both UHD and LD DACs

Recent studies show that the spin magnetic moment of the active center as an intrinsic physical property, can be a good activity descriptor for the ORR on SACs [93]. For example, the larger spin magnetic moments can induce better catalytic activity for the ORR on the $\mathrm{FeN_4}$-based SACs because the spin electrons are beneficial for binding and activation of reaction intermediates [94]. Correspondingly, we investigate the possibility of the spin magnetic moment as an ORR activity descriptor herein. Interestingly, as shown in Fig. 5(a), $\Delta G(^*\mathrm{OH})$ for all UHD and LD DAC systems is correlated linearly with the spin magnetic moment, M_S, of the metal atom that binds OH ($R^2 = 0.87$), which shows that the larger spin magnetic moment contributes to the stronger adsorption of *OH. This strong linear correlation suggests that M_S can function as an efficient descriptor to predict the ORR catalytic activity. As expected, as shown in Fig. 5(b), η_{ORR} indeed exhibits a volcano relationship with M_S and, importantly, M_S is a unified descriptor for both UHD and LD DAC systems.

Importantly, the excellent linear relationship between $\Delta G(^*\mathrm{OH})$ and M_S, and volcano relationship between $\Delta G(^*\mathrm{OH})$ and η_{ORR}, are also confirmed by the HSE06 functional (Fig. S19 within the Supplemental Material [31]). From Figs. S19(a) and S19(c) within the Supplemental Material [31], there is a good linear scaling relationship between M_S and $\Delta G(^*\mathrm{OH})$ for both PBE and HSE methods, with linear slopes of -0.47 and -0.35, respectively. The relatively smaller M_S for the magnetic active center obtained by the PBE method is responsible for the more negative slope, compared with that from the HSE method. Moreover, there is a good volcanic relationship for η_{ORR} as a function of M_S for PBE and HSE calculations [Figs. S19(b) and S19(d) within the Supplemental Material [31]]. It is found that the critical M_S corresponding to the theoretical optimal activity obtained by PBE ($0.94\mu_B$) is smaller than that based on the HSE functional ($1.32\mu_B$), which also stems from the smaller M_S for the magnetic active center obtained by the PBE method. These results suggest

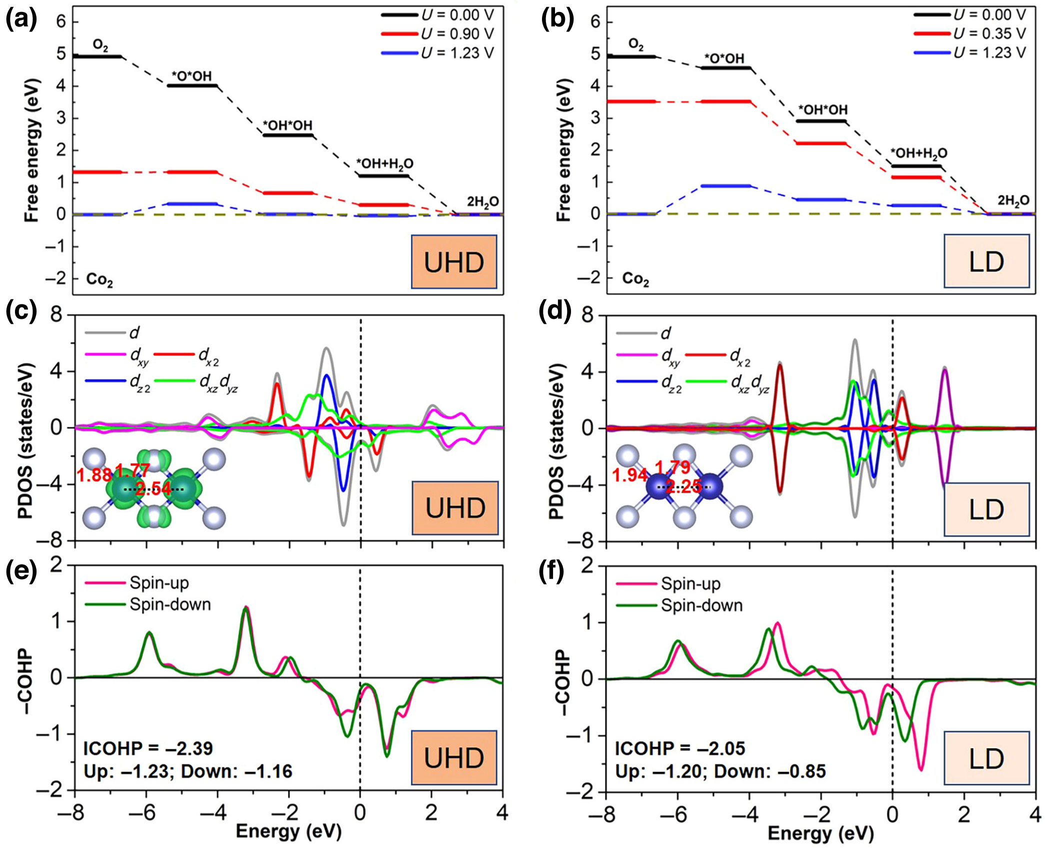

FIG. 6. Reaction free-energy diagrams of the ORR for Co_2N_6 (a) UHD and (b) LD DACs at different potentials for optimal pathway C. PDOS of Co 3*d* orbitals for Co_2N_6 (c) UHD and (d) LD DACs without *OH adsorption. Here, Fermi level is set to 0. Inset figure is the corresponding spin density (0.005 e/bohr^3) for Co_2N_6 UHD and LD DACs. COHP for the interaction between Co and *OH for (e) UHD and (f) LD DACs.

that the spin-related conclusions are reliable from the PBE method, and, as one of the key points in our work, the spin magnetic moment of the active center obtained with the PBE functional can indeed act as a catalytic descriptor for the ORR on the DACs, similar to that of the HSE functional.

Finally, we explore the mechanism for the significantly enhanced ORR activity of the Co_2N_6 UHD DAC compared with its LD DAC counterpart, for which the free-energy diagrams are presented in Figs. 6(a) and 6(b). From above, we know that the excellent ORR activity of the Co_2N_6 UHD DAC results from its proper binding of *OH, which correlates with the spin magnetic moment of the active center. Therefore, we comparatively study the spin magnetic states of the Co_2N_6 UHD DAC and LD DAC. As presented in Figs. 6(c) and 6(d), the PDOS show that the Co 3*d* orbitals are asymmetric in the UHD DAC system but symmetric in the LD DAC system, indicating the (non)magnetic states of Co atoms for (LD) UHD DAC. Moreover, the Co d_{x^2}, d_{xz}, and d_{yz} in-plane orbitals mainly contribute to the spin magnetic moment of the Co atom in the UHD DAC.

Based on crystal-field theory, the Co cation in the CoN_4 square-planar crystal field for the SAC system possesses the 3d^7-electron configuration [95], which should have unpaired electrons and give rise to the spin magnetic state. However, in the current DAC systems, there are double CoN_4 square-planar crystal fields interacting with each other. For the Co_2N_6 LD DAC, the short Co-Co distance (2.25 Å) can intensively share the *d*-orbital electrons, resulting in the faultless pairing of in-plane *d*-orbital electrons (d_{x^2}, d_{xz}, and d_{yz}) and the complete quenching of the spin magnetic moment in the LD DAC. In contrast, a large Co-Co distance (2.54 Å) in the UHD DAC contributes to retention of the spin magnetic moment. The spin-density distributions illustrated in Figs. 6(c) and 6(d) can also confirm our above analysis of the difference in the spin magnetic states between Co_2N_6 UHD and LD DACs.

In addition, we study the electronic state interactions between Co 3*d* and *OH 2*sp*, for which the PDOS are presented in Fig. S20 within the Supplemental Material [31], and furthermore, a quantitative analysis is given in Figs. 6(e) and 6(f), resulting from the crystal orbital Hamilton populations (COHP). For the Co_2N_6 UHD DAC, the adsorption of *OH almost leads to complete spin quenching of the Co atom that binds it (see Fig. S20 within the Supplemental Material [31]), and thus, the spin-up and spin-down bands contribute similar binding strengths with integrated COHP (ICOHP) of -1.23 and -1.16 eV, respectively. On the contrary, for the Co_2N_6 LD DAC, the adsorption of *OH can induce a spin magnetic moment on the Co atoms. Significantly, spin-up bands contribute similar binding strengths, compared with the case of the Co_2N_6 UHD DAC, with ICOHP of -1.20 eV, while much higher occupation of the antibonding state for spin-down bands leads to the much smaller contribution to *OH binding, with ICOHP of -0.85 eV. Consequently, the Co_2N_6 UHD DAC binds *OH more strongly than the Co_2N_6 UHD DAC and exhibits high ORR activity.

IV. CONCLUSIONS

We theoretically confirm the existence of ultrahigh-density DACs, with a metal loading of >40 wt %, constructed from the experimentally synthesized M_2N_6 motif. Among the investigated systems, ten (Mn_2N_6, Fe_2N_6, Co_2N_6, Ni_2N_6, $MnFeN_6$, $MnCoN_6$, $MnNiN_6$, $FeCoN_6$, $FeNiN_6$, and $CoNiN_6$) are demonstrated to have good dynamic, thermal, mechanical, thermodynamic, and electrochemical stabilities. Mechanistic studies of the ORR show that most of the UHD DACs have comparable ORR activities to the corresponding LD DACs, and Fe_2N_6 and Co_2N_6 UHD DACs are located at the peak of the activity volcano with ultralow overpotentials of 0.31 and 0.33 V, respectively. Furthermore, we investigate the relationship between the ORR activities and spin states of the active centers and identify that the spin magnetic moment of the active centers of the DACs can serve as an effective catalytic descriptor. Interestingly, Co_2N_6 UHD DACs exhibit significantly enhanced ORR activity compared with their Co_2N_6 LD counterparts, which can be ascribed to distortion of the square-planar crystal-field-induced spin-state crossover. In addition, the simulated STM images and symmetry classifications of phonon modes for the UHD DAC systems provide a basis for future experimental confirmation. We hope our prediction will stimulate the experimental exploration of ultrahigh-density DACs for practical catalytic applications, and the identified activity descriptor—spin magnetic moment—will guide the rational design of efficient DACs based on spin-state regulation.

ACKNOWLEDGMENTS

This work is supported by the National Natural Science Foundation of China (Grants No. 12204151 and 12274118), the Program for Science & Technology Innovation Talents in Universities of Henan Province (Grant No. 20HASTIT028), the Special Project for Fundamental Research in University of Henan Province (Grant No. 22ZX013), the China Postdoctoral Science Foundation (Grant No. 2022M711048), and its Matching Fund from Henan province (Grant No, J23029Y) and the Open Project Program of Guangdong Provincial Key Laboratory of Electronic Functional Materials and Devices, Huizhou University (Grant No. EFMD2022009M), and Henan Center for Outstanding Overseas Scientists (Grant No. GZS2023007). The work is carried out at the National Supercomputer Center in Tianjin, and this research is supported by the TianHe Qingsuo Project Special Fund Project.

[1] A. Kulkarni, S. Siahrostami, A. Patel, and J. K. Nørskov, Understanding catalytic activity trends in the oxygen reduction reaction, Chem. Rev. **118**, 2302 (2018).

[2] R. Chattot, O. Le Bacq, V. Beermann, S. Kühl, J. Herranz, S. Henning, L. Kühn, T. Asset, L. Guétaz, G. Renou, *et al.*, Surface distortion as a unifying concept and descriptor in oxygen reduction reaction electrocatalysis, Nat. Mater. **17**, 827 (2018).

[3] X. Tian, X. F. Lu, B. Y. Xia, and X. W. (David) Lou, Advanced electrocatalysts for the oxygen reduction reaction in energy conversion technologies, Joule **4**, 45 (2020).

[4] X. Huang, Z. Zhao, L. Cao, Y. Chen, E. Zhu, Z. Lin, M. Li, A. Yan, A. Zettl, Y. M. Wang, *et al.*, High-performance transition metal–doped Pt_3Ni octahedra for oxygen reduction reaction, Science **348**, 1230 (2015).

[5] M. Li, Z. Zhao, T. Cheng, A. Fortunelli, C.-Y. Chen, R. Yu, Q. Zhang, L. Gu, B. V. Merinov, Z. Lin, *et al.*, Ultrafine jagged platinum nanowires enable ultrahigh mass activity for the oxygen reduction reaction, Science **354**, 1414 (2016).

[6] X. Yang, X. Zhang, Z. Lu, Z. Yang, and R. Wu, Design of Highly Stable and Efficient Bifunctional MXene-Based Electrocatalysts for Oxygen Reduction and Evolution Reactions, Phys. Rev. Appl. **15**, 044053 (2021).

[7] U. Martinez, S. Komini Babu, E. F. Holby, H. T. Chung, X. Yin, and P. Zelenay, Progress in the development of Fe-based PGM-free electrocatalysts for the oxygen reduction reaction, Adv. Mater. **31**, 1806545 (2019).

[8] X. F. Lu, Y. Fang, D. Luan, and X. W. D. Lou, Metal–organic frameworks derived functional materials for electrochemical energy storage and conversion: A mini review, Nano Lett. **21**, 1555 (2021).

[9] S. Liu, C. Li, M. J. Zachman, Y. Zeng, H. Yu, B. Li, M. Wang, J. Braaten, J. Liu, H. M. Meyer, *et al.*, Atomically dispersed iron sites with a nitrogen–carbon coating as highly active and durable oxygen reduction catalysts for fuel cells, Nat. Energy **7**, 652 (2022).

[10] W. Zhang, Q. Fu, Q. Luo, L. Sheng, and J. Yang, Understanding single-atom catalysis in view of theory, JACS Au **1**, 2130 (2021).

[11] C. Tang, L. Chen, H. Li, L. Li, Y. Jiao, Y. Zheng, H. Xu, K. Davey, and S.-Z. Qiao, Tailoring acidic oxygen reduction selectivity on single-atom catalysts via modification of first and second coordination spheres, J. Am. Chem. Soc. **143**, 7819 (2021).

[12] C. Zhu, Q. Shi, B. Z. Xu, S. Fu, G. Wan, C. Yang, S. Yao, J. Song, H. Zhou, D. Du, *et al.*, Hierarchically porous M–N–C(M = Co and Fe) single-atom electrocatalysts with robust MN$_x$ active moieties enable enhanced ORR performance, Adv. Energy Mater. **8,** 1801956 (2018).

[13] J. Kim, J. M. Yoo, H. S. Lee, Y.-E. Sung, and T. Hyeon, Single-atom M–N–C catalysts for oxygen reduction electrocatalysis, Trends Chem. **3**, 779 (2021).

[14] J. Liu, X. Wan, S. Liu, X. Liu, L. Zheng, R. Yu, and J. Shui, Hydrogen passivation of M–N–C(M = Fe, Co) catalysts for storage stability and ORR activity improvements, Adv. Mater. **33**, 2103600 (2021).

[15] Y. Wang, X. Cui, J. Zhang, J. Qiao, H. Huang, J. Shi, and G. Wang, Advances of atomically dispersed catalysts from single-atom to clusters in energy storage and conversion applications, Prog. Mater. Sci. **128**, 100964 (2022).

[16] Y. Ying, X. Luo, J. Qiao, and H. Huang, "More is different:" Synergistic effect and structural engineering in double-atom catalysts, Adv. Funct. Mater. **31**, 2007423 (2021).

[17] R. Li and D. Wang, Superiority of dual-atom catalysts in electrocatalysis: One step further than single-atom catalysts, Adv. Energy Mater. **12**, 2103564 (2022).

[18] W. Zou, R. Lu, X. Liu, G. Xiao, X. Liao, Z. Wang, and Y. Zhao, Theoretical insights into dual-atom catalysts for the oxygen reduction reaction: The crucial role of orbital polarization, J. Mater. Chem. A **10**, 9150 (2022).

[19] J. Wang, Z. Huang, W. Liu, C. Chang, H. Tang, Z. Li, W. Chen, C. Jia, T. Yao, S. Wei, *et al.*, Design of N-coordinated dual-metal sites: A stable and active Pt-free catalyst for acidic oxygen reduction reaction, J. Am. Chem. Soc. **139**, 17281 (2017).

[20] Y. He, X. Yang, Y. Li, L. Liu, S. Guo, C. Shu, F. Liu, Y. Liu, Q. Tan, and G. Wu, Atomically dispersed Fe–Co dual metal sites as bifunctional oxygen electrocatalysts for rechargeable and flexible Zn–air batteries, ACS Catal. **12**, 1216 (2022).

[21] Q. An, J. Jiang, W. Cheng, H. Su, Y. Jiang, and Q. Liu, Recent advances in dual-atom site catalysts for efficient oxygen and carbon dioxide electrocatalysis, Small Methods **6**, 2200408 (2022).

[22] J. Zhang, A. Yu, and C. Sun, Computational exploration of dual atom catalysts loaded on defective graphene for oxygen reduction reaction, Appl. Surf. Sci. **605**, 154534 (2022).

[23] Y. Zhou, W. Yang, W. Utetiwabo, Y. Lian, X. Yin, L. Zhou, P. Yu, R. Chen, and S. Sun, Revealing of active sites and catalytic mechanism in N-coordinated Fe, Ni dual-doped carbon with superior acidic oxygen reduction than single-atom catalyst, J. Phys. Chem. Lett. **11**, 1404 (2020).

[24] G. Yang, J. Zhu, P. Yuan, Y. Hu, G. Qu, B.-A. Lu, X. Xue, H. Yin, W. Cheng, J. Cheng, *et al.*, Regulating Fe-spin state by atomically dispersed Mn-N in Fe-N-C catalysts with high oxygen reduction activity, Nat. Commun. **12**, 1734 (2021).

[25] H. Li, S. Di, P. Niu, S. Wang, J. Wang, and L. Li, A durable half-metallic diatomic catalyst for efficient oxygen reduction, Energy Environ. Sci. **15**, 1601 (2022).

[26] X. Zhou, J. Gao, Y. Hu, Z. Jin, K. Hu, K. M. Reddy, Q. Yuan, X. Lin, and H.-J. Qiu, Theoretically revealed and experimentally demonstrated synergistic electronic interaction of CoFe dual-metal sites on N-doped carbon for boosting both oxygen reduction and evolution reactions, Nano Lett. **22**, 3392 (2022).

[27] M. Liu, H. Chun, T.-C. Yang, S. J. Hong, C.-M. Yang, B. Han, and L. Y. S. Lee, Tuning the site-to-site interaction in Ru–M (M = Co, Fe, Ni) diatomic electrocatalysts to climb up the volcano plot of oxygen electroreduction, ACS Nano **16**, 10657 (2022).

[28] J. Yan, M. Tian, R. Shi, T. Gu, K. Zeng, J. Zhou, Q. Zhang, M. H. Rümmeli, and R. Yang, Enhanced dual atomic Fe-Ni sites in N-doped carbon for bifunctional oxygen electrocatalysis, Mater. Today Energy **30**, 101171 (2022).

[29] H. Li, J. Wang, R. Qi, Y. Hu, J. Zhang, H. Zhao, J. Zhang, and Y. Zhao, Enhanced Fe 3d delocalization and moderate spin polarization in FeNi atomic pairs for bifunctional ORR and OER electrocatalysis, Appl. Catal. B **285**, 119778 (2021).

[30] F. Wang, W. Xie, L. Yang, D. Xie, and S. Lin, Revealing the importance of kinetics in N-coordinated dual-metal sites catalyzed oxygen reduction reaction, J Catal. **396**, 215 (2021).

[31] See the Supplemental Material at http://link.aps.org/supplemental/10.1103/PhysRevApplied.19.054094 for more details of structural parameters, the atomic model, simulation results, scaling relationship of adsorption for key intermediates, free energy diagrams, selectivity analysis, and solvation-effect analysis for different adsorbed species, as well as Refs. [18,58,59,67–71].

[32] Y. Meng, C. Yin, K. Li, H. Tang, Y. Wang, and Z. Wu, Improved oxygen reduction activity in heteronuclear FeCo-Co-doped graphene: A theoretical study, ACS Sustainable Chem. Eng. **7**, 17273 (2019).

[33] Y. Sun, J. Wang, Q. Liu, M. Xia, Y. Tang, F. Gao, Y. Hou, J. Tse, and Y. Zhao, Itinerant ferromagnetic half metallic cobalt–iron couples: Promising bifunctional electrocatalysts for ORR and OER, J. Mater. Chem. A **7**, 27175 (2019).

[34] C. Liu, T. Li, X. Dai, J. Zhao, D. He, G. Li, B. Wang, and X. Cui, Catalytic activity enhancement on alcohol dehydrogenation via directing reaction pathways from single- to double-atom catalysis, J. Am. Chem. Soc. **144**, 4913 (2022).

[35] Y. Wang, B. J. Park, V. K. Paidi, R. Huang, Y. Lee, K.-J. Noh, K.-S. Lee, and J. W. Han, Precisely constructing orbital coupling-modulated dual-atom Fe pair sites for synergistic CO$_2$ electroreduction, ACS Energy Lett. **7**, 640 (2022).

[36] N. Karmodak, S. Vijay, G. Kastlunger, and K. Chan, Computational screening of single and di-atom catalysts for electrochemical CO$_2$ reduction, ACS Catal. **12**, 4818 (2022).

[37] J. Hao, Z. Zhuang, J. Hao, C. Wang, S. Lu, F. Duan, F. Xu, M. Du, and H. Zhu, Interatomic electronegativity offset dictates selectivity when catalyzing the CO$_2$ reduction reaction, Adv. Energy Mater. **12**, 2200579 (2022).

[38] F. Li and Q. Tang, Understanding trends in the activity and selectivity of Bi-atom catalysts for the electrochemical

reduction of carbon dioxide, J. Mater. Chem. A **9**, 8761 (2021).

[39] T. Ding, X. Liu, Z. Tao, T. Liu, T. Chen, W. Zhang, X. Shen, D. Liu, S. Wang, B. Pang, *et al.*, Atomically precise dinuclear site active toward electrocatalytic CO_2 reduction, J. Am. Chem. Soc. **143**, 11317 (2021).

[40] B. Qiao, A. Wang, X. Yang, L. F. Allard, Z. Jiang, Y. Cui, J. Liu, J. Li, and T. Zhang, Single-atom catalysis of CO oxidation using Pt_1/FeO_x, Nat. Chem. **3**, 634 (2011).

[41] P. Liu, Y. Zhao, R. Qin, S. Mo, G. Chen, L. Gu, D. M. Chevrier, P. Zhang, Q. Guo, D. Zang, *et al.*, Photochemical route for synthesizing atomically dispersed palladium catalysts, Science **352**, 797 (2016).

[42] J.-C. Liu, H. Xiao, and J. Li, Constructing high-loading single-atom/cluster catalysts via an electrochemical potential window strategy, J. Am. Chem. Soc. **142**, 3375 (2020).

[43] Y. Li, W. Shan, M. J. Zachman, M. Wang, S. Hwang, H. Tabassum, J. Yang, X. Yang, S. Karakalos, Z. Feng, *et al.*, Atomically dispersed dual-metal site catalysts for enhanced CO_2 reduction: Mechanistic insight into active site structures, Angew. Chem., Int. Ed. **61**, e202205632 (2022).

[44] L. Zhao, Y. Zhang, L.-B. Huang, X.-Z. Liu, Q.-H. Zhang, C. He, Z.-Y. Wu, L.-J. Zhang, J. Wu, W. Yang, *et al.*, Cascade anchoring strategy for general mass production of high-loading single-atomic metal-nitrogen catalysts, Nat. Commun. **10**, 1278 (2019).

[45] C. Tang, Y. Jiao, B. Shi, J.-N. Liu, Z. Xie, X. Chen, Q. Zhang, and S.-Z. Qiao, Coordination tunes selectivity: Two-electron oxygen reduction on high-loading molybdenum single-atom catalysts, Angew. Chem., Int. Ed. **59**, 9171 (2020).

[46] S. Tian, C. Peng, J. Dong, Q. Xu, Z. Chen, D. Zhai, Y. Wang, L. Gu, P. Hu, H. Duan, *et al.*, High-loading single-atomic-site silver catalysts with an Ag_1–C_2N_1 structure showing superior performance for epoxidation of styrene, ACS Catal. **11**, 4946 (2021).

[47] J. Li, W. Xia, J. Tang, Y. Gao, C. Jiang, Y. Jia, T. Chen, Z. Hou, R. Qi, D. Jiang, *et al.*, Metal–organic framework-derived graphene mesh: A robust scaffold for highly exposed Fe–N_4 active sites toward an excellent oxygen reduction catalyst in acid media, J. Am. Chem. Soc. **144**, 9280 (2022).

[48] Y. Xiong, W. Sun, P. Xin, W. Chen, X. Zheng, W. Yan, L. Zheng, J. Dong, J. Zhang, D. Wang, *et al.*, Gram-scale synthesis of high-loading single-atomic-site Fe catalysts for effective epoxidation of styrene, Adv. Mater. **32**, 2000896 (2020).

[49] Y. Zhou, X. Tao, G. Chen, R. Lu, D. Wang, M.-X. Chen, E. Jin, J. Yang, H.-W. Liang, Y. Zhao, *et al.*, Multilayer stabilization for fabricating high-loading single-atom catalysts, Nat. Commun. **11**, 5892 (2020).

[50] X. Hai, S. Xi, S. Mitchell, K. Harrath, H. Xu, D. F. Akl, D. Kong, J. Li, Z. Li, T. Sun, *et al.*, Scalable two-step annealing method for preparing ultra-high-density single-atom catalyst libraries, Nat. Nanotech. **17**, 174 (2022).

[51] C. Xia, Y. Qiu, Y. Xia, P. Zhu, G. King, X. Zhang, Z. Wu, J. Y. (Timothy) Kim, D. A. Cullen, D. Zheng, *et al.*, General synthesis of single-atom catalysts with high metal loading using graphene quantum dots, Nat. Chem. **13**, 887 (2021).

[52] J. P. Perdew, K. Burke, and M. Ernzerhof, Generalized Gradient Approximation Made Simple, Phys. Rev. Lett. **77**, 3865 (1996).

[53] G. Kresse and J. Furthmüller, Efficient iterative schemes for *ab initio* total-energy calculations using a plane-wave basis set, Phys. Rev. B **54**, 11169 (1996).

[54] G. Kresse and J. Furthmüller, Efficiency of *ab-initio* total energy calculations for metals and semiconductors using a plane-wave basis set, Comput. Mater. Sci. **6**, 15 (1996).

[55] S. Grimme, J. Antony, S. Ehrlich, and H. Krieg, A consistent and accurate *ab initio* parametrization of density functional dispersion correction (DFT-D) for the 94 elements H-Pu, J. Chem. Phys. **132**, 154104 (2010).

[56] A. Togo, F. Oba, and I. Tanaka, First-principles calculations of the ferroelastic transition between rutile-type and $CaCl_2$-type SiO_2 at high pressures, Phys. Rev. B **78**, 134106 (2008).

[57] J. Tersoff and D. R. Hamann, Theory and Application for the Scanning Tunneling Microscope, Phys. Rev. Lett. **50**, 1998 (1983).

[58] J. Greeley and J. K. Nørskov, Electrochemical dissolution of surface alloys in acids: Thermodynamic trends from first-principles calculations, Electrochim. Acta **52**, 5829 (2007).

[59] X. Guo, S. Lin, J. Gu, S. Zhang, Z. Chen, and S. Huang, Simultaneously achieving high activity and selectivity toward two-electron O_2 electroreduction: The power of single-atom catalysts, ACS Catal. **9**, 11042 (2019).

[60] X. Lv, W. Wei, B. Huang, Y. Dai, and T. Frauenheim, High-throughput screening of synergistic transition metal dual-atom catalysts for efficient nitrogen fixation, Nano Lett. **21**, 1871 (2021).

[61] Q. Wei and X. Peng, Superior mechanical flexibility of phosphorene and few-layer black phosphorus, Appl. Phys. Lett. **104**, 251915 (2014).

[62] A. A. Peterson, F. Abild-Pedersen, F. Studt, J. Rossmeisl, and J. K. Nørskov, How copper catalyzes the electroreduction of carbon dioxide into hydrocarbon fuels, Energy Environ. Sci. **3**, 1311 (2010).

[63] J. K. Nørskov, J. Rossmeisl, A. Logadottir, L. Lindqvist, J. R. Kitchin, T. Bligaard, and H. Jónsson, Origin of the overpotential for oxygen reduction at a fuel-cell cathode, J. Phys. Chem. B **108**, 17886 (2004).

[64] J. Rossmeisl, A. Logadottir, and J. K. Nørskov, Electrolysis of water on (oxidized) metal surfaces, Chem. Phys. **319**, 178 (2005).

[65] http://Webbook.Nist.Gov/Chemistry/, (n.d.).

[66] V. Wang, N. Xu, J.-C. Liu, G. Tang, and W.-T. Geng, VASPKIT: A user-friendly interface facilitating high-throughput computing and analysis using VASP code, Comp. Phys. Commun. **267**, 108033 (2021).

[67] K. Mathew, R. Sundararaman, K. Letchworth-Weaver, T. A. Arias, and R. G. Hennig, Implicit solvation model for density-functional study of nanocrystal surfaces and reaction pathways, J. Chem. Phys. **140**, 084106 (2014).

[68] G. Xiao, R. Lu, J. Liu, X. Liao, Z. Wang, and Y. Zhao, Coordination environments tune the activity of oxygen catalysis on single atom catalysts: A computational study, Nano Res. **15**, 3073 (2022).

[69] S. Plimpton, Fast parallel algorithms for short-range molecular dynamics, J. Comput. Phys. **117**, 1 (1995).

[70] W. L. Jorgensen, J. Chandrasekhar, J. D. Madura, R. W. Impey, and M. L. Klein, Comparison of simple potential functions for simulating liquid water, J. Chem. Phys. **79**, 926 (1983).

[71] M. Reda, H. A. Hansen, and T. Vegge, DFT study of stabilization effects on N-doped graphene for ORR catalysis, Catal. Today **312**, 118 (2018).

[72] T. Jing, T. Li, D. Rao, M. Wang, and Y. Zuo, Defining the loading of single-atom catalysts: Weight fraction or atomic fraction?, Mater. Today Energy **31**, 101197 (2023).

[73] J. Ibaceta-Jaña, R. Muydinov, P. Rosado, H. Mirhosseini, M. Chugh, O. Nazarenko, D. N. Dirin, D. Heinrich, M. R. Wagner, T. D. Kühne, *et al.*, Vibrational dynamics in lead halide hybrid perovskites investigated by Raman spectroscopy, Phys. Chem. Chem. Phys. **22**, 5604 (2020).

[74] Y. Le Page and P. Saxe, Symmetry-general least-squares extraction of elastic data for strained materials from *ab initio* calculations of stress, Phys. Rev. B **65**, 104104 (2002).

[75] F. Liu, P. Ming, and J. Li, *Ab initio* calculation of ideal strength and phonon instability of graphene under tension, Phys. Rev. B **76**, 064120 (2007).

[76] F. Mouhat and F.-X. Coudert, Necessary and sufficient elastic stability conditions in various crystal systems, Phys. Rev. B **90**, 224104 (2014).

[77] P. Lv, G. Tang, C. Yang, J. Deng, Y. Liu, X. Wang, X. Wang, and J. Hong, Half-metallicity in two-dimensional Co_2Se_3 monolayer with superior mechanical flexibility, 2D Mater. **5**, 045026 (2018).

[78] C. Lee, X. Wei, J. W. Kysar, and J. Hone, Measurement of the elastic properties and intrinsic strength of monolayer graphene, Science **321**, 385 (2008).

[79] Y. Yang, Y. Xue, H. Zhang, and H. Chang, Flexible H_2O_2 microfluidic fuel cell using graphene/Prussian blue catalyst for high performance, Chem. Eng. J. **369**, 813 (2019).

[80] X. Guo, J. Gu, S. Lin, S. Zhang, Z. Chen, and S. Huang, Tackling the activity and selectivity challenges of electrocatalysts toward the nitrogen reduction reaction via atomically dispersed biatom catalysts, J. Am. Chem. Soc. **142**, 5709 (2020).

[81] D. Ma, Y. Wang, L. Liu, and Y. Jia, Electrocatalytic nitrogen reduction on the transition-metal dimer anchored N-doped graphene: Performance prediction and synergetic effect, Phys. Chem. Chem. Phys. **23**, 4018 (2021).

[82] P. Lv, D. Wu, B. He, X. Li, R. Zhu, G. Tang, Z. Lu, D. Ma, and Y. Jia, An efficient screening strategy towards multifunctional catalysts for the simultaneous electroreduction of NO_3^-, NO_2^- and NO to NH_3, J. Mater. Chem. A **10**, 9707 (2022).

[83] J. Paier, M. Marsman, K. Hummer, G. Kresse, I. C. Gerber, and J. G. Ángyán, Screened hybrid density functionals applied to solids, J. Chem. Phys. **124**, 154709 (2006).

[84] L. Li, B. Huang, X. Tang, Y. Hong, W. Zhai, T. Hu, K. Yuan, and Y. Chen, Recent developments of microenvironment engineering of single-atom catalysts for oxygen reduction toward desired activity and selectivity, Adv. Funct. Mater. **31**, 2103857 (2021).

[85] Z. Qin and J. Zhao, $1T$-$MoSe_2$ monolayer supported single Pd atom as a highly-efficient bifunctional catalyst for ORR/OER, J. Colloid Interface Sci. **605**, 155 (2022).

[86] L. Yu, F. Li, J. Zhao, and Z. Chen, Revisiting catalytic performance of supported metal dimers for oxygen reduction reaction via magnetic coupling from first principles, Adv. Powder Mater. **1**, 100031 (2022).

[87] D. Wu, B. He, Y. Wang, P. Lv, D. Ma, and Y. Jia, Double-atom catalysts for energy-related electrocatalysis applications: A theoretical perspective, J. Phys. D: Appl. Phys. **55**, 203001 (2022).

[88] C. H. Choi, H.-K. Lim, M. W. Chung, J. C. Park, H. Shin, H. Kim, and S. I. Woo, Long-range electron transfer over graphene-based catalyst for high-performing oxygen reduction reactions: Importance of size, N-doping, and metallic impurities, J. Am. Chem. Soc. **136**, 9070 (2014).

[89] H. Li, Z. Zhao, Q. Cai, L. Yin, and J. Zhao, Nitrogen electroreduction performance of transition metal dimers embedded into N-doped graphene: A theoretical prediction, J. Mater. Chem. A **8**, 4533 (2020).

[90] S. Wang, L. Shi, X. Bai, Q. Li, C. Ling, and J. Wang, Highly efficient photo-/electrocatalytic reduction of nitrogen into ammonia by dual-metal sites, ACS Cent. Sci. **6**, 1762 (2020).

[91] Y. Ouyang, L. Shi, X. Bai, Q. Li, and J. Wang, Breaking scaling relations for efficient CO_2 electrochemical reduction through dual-atom catalysts, Chem. Sci. **11**, 1807 (2020).

[92] H. A. Hansen, J. Rossmeisl, and J. K. Nørskov, Surface Pourbaix diagrams and oxygen reduction activity of Pt, Ag and Ni(111) surfaces studied by DFT, Phys. Chem. Chem. Phys. **10**, 3722 (2008).

[93] W. Zhong, Y. Qiu, H. Shen, X. Wang, J. Yuan, C. Jia, S. Bi, and J. Jiang, Electronic spin moment as a catalytic descriptor for Fe single-atom catalysts supported on C_2N, J. Am. Chem. Soc. **143**, 4405 (2021).

[94] R. Wang, L. Zhang, J. Shan, Y. Yang, J.-F. Lee, T.-Y. Chen, J. Mao, Y. Zhao, L. Yang, Z. Hu, *et al.*, Tuning Fe spin moment in Fe–N–C catalysts to climb the activity volcano via a local geometric distortion strategy, Adv. Sci. **9**, 2203917 (2022).

[95] Z. Duan and G. Henkelman, Surface charge and electrostatic spin crossover effects in CoN_4 electrocatalysts, ACS Catal. **10**, 12148 (2020).